



Impact of Magnetorotational Instability on Grain Growth in Protoplanetary Disks. II. Increased Grain Collisional Velocities

Munan Gong¹ , Alexei V. Ivlev¹ , Vitaly Akimkin² , and Paola Caselli¹

¹ Max-Planck Institute for Extraterrestrial Physics, Garching by Munich, D-85748, Germany; munan@mpe.mpg.de

² Institute of Astronomy, Russian Academy of Sciences, Pyatnitskaya str. 48, Moscow, 119017, Russia

Received 2021 May 11; revised 2021 June 17; accepted 2021 June 17; published 2021 August 20

Abstract

Turbulence is the dominant source of collisional velocities for grains with a wide range of sizes in protoplanetary disks. So far, only Kolmogorov turbulence has been considered for calculating grain collisional velocities, despite the evidence that turbulence in protoplanetary disks may be non-Kolmogorov. In this work, we present calculations of grain collisional velocities for arbitrary turbulence models characterized by power-law spectra and determined by three dimensionless parameters: the slope of the kinetic energy spectrum, the slope of the autocorrelation time, and the Reynolds number. The implications of our results are illustrated by numerical simulations of the grain size evolution for different turbulence models. We find that for the modeled cases of the Iroshnikov–Kraichnan turbulence and the turbulence induced by the magnetorotational instabilities, collisional velocities of small grains are much larger than those for the standard Kolmogorov turbulence. This leads to faster grain coagulation in the outer regions of protoplanetary disks, resulting in rapid increase of dust opacity in millimeter wavelength and possibly promoting planet formation in very young disks.

Unified Astronomy Thesaurus concepts: [Interstellar dust \(836\)](#); [Protoplanetary disks \(1300\)](#)

1. Introduction

Interstellar dust grains play an important role in many aspects of astrophysics: they are building blocks of planets, commonly used gas tracers, and catalysts of molecular chemistry. All these processes depend on the size distribution of dust grains, and great efforts have been made to model the process of grain growth, especially in protoplanetary disks (see reviews by Blum & Wurm 2008; Testi et al. 2014; Birnstiel et al. 2016). In various astrophysical environments, turbulence is the major driving force for grain growth. Turbulent motions stir up the grains, leading to their mutual collisions. In protoplanetary disks, for example, turbulence is among the dominant sources for collisional velocities between grains in the size range of microns to meters (Birnstiel et al. 2011).

The calculation of grain collisional velocity induced by turbulence generally relies on one critical assumption: the turbulence is Kolmogorov with a kinetic energy spectrum of $E(k) \propto k^{-5/3}$. Völk et al. (1980) and Markiewicz et al. (1991) made the ground-laying work of calculating grain collisional velocities in Kolmogorov turbulence. Later Ormel & Cuzzi (2007, hereafter OC2007) derived the analytic expressions for grain collisional velocities in Kolmogorov turbulence, which were soon adopted in many grain coagulation codes (e.g., Brauer et al. 2008; Okuzumi et al. 2012; Akimkin et al. 2020b). The grain collisional velocities derived from these analytic Völk-type models were tested by direct numerical simulations in Pan & Padoan (2015), Ishihara et al. (2018), and Sakurai et al. (2021). The simulations showed that while Völk-type models suffer from several drawbacks, such as the neglect of turbulent clustering of same-size grains (which enhances their collisional rates) and a reduction of the rms collisional velocity (which reduces the collisional rates), the overall grain collisional velocities derived from Völk-type models are still accurate within a factor of ~ 2 . With its relative accuracy and simplicity, the formulae in OC2007 remain the standard adopted in the current literature.

The astrophysical turbulence, however, does not necessarily have the Kolmogorov spectrum. The presence of magnetic fields is expected to change the turbulence cascade, and many alternative theories have been proposed to describe the magnetohydrodynamic (MHD) turbulence. The Iroshnikov–Kraichnan (IK) theory, for example, predicts $E(k) \propto k^{-3/2}$ (Iroshnikov 1964; Kraichnan 1965). Alternatively, the Goldreich–Sridhar theory predicts $E(k_{\parallel}) \propto k_{\parallel}^{-2}$ parallel to the mean magnetic field and $E(k_{\perp}) \propto k_{\perp}^{-5/3}$ perpendicular to the mean magnetic field (Goldreich & Sridhar 1995). These theories, however, assume that there is a dominant mean magnetic field. In many astrophysical environments such as the protoplanetary disks, the magnetic field is weak and the mean field varies on spatial and temporal scales of the turbulent cascade. It is unclear whether the theoretical predictions by the IK or Goldreich–Sridhar turbulence models still hold in these environments.

In our previous paper (Gong et al. 2020, hereafter Paper I), we performed numerical simulations of the MHD turbulence in protoplanetary disks generated by the magnetorotational instabilities (MRIs). We observed a persistent kinetic energy spectrum of $k^{-4/3}$, which appears to be converged in terms of numerical resolution. This $k^{-4/3}$ energy spectrum has also been observed in many other MHD turbulence simulations in the literature (see Table 6 in Paper I). To further investigate this phenomenon, we also performed driven turbulence simulations with and without the magnetic field and obtained the same energy spectrum. We concluded that the $k^{-4/3}$ power-law slope is likely due to the bottleneck effect near the dissipation scale of the turbulence (Ishihara et al. 2016). Due to the limited numerical resolution, we were not able to constrain whether the $k^{-4/3}$ energy spectrum extends to a larger dynamical range. In addition, we found the turbulence autocorrelation time to vary close to $\propto k^{-1}$, which is steeper than that for the Kolmogorov turbulence. Moreover, the injection scale of the MRI turbulence is determined by the fastest-growing mode of the MRI—not by the scale height of the disk assumed as the injection scale.

in OC2007. All these factors—the energy spectrum, the autocorrelation time, and the injection scale of the turbulence—can have a big impact on the grain collisional velocities.

Recently, Grete et al. (2021) performed numerical simulations of weakly magnetized MHD turbulence and found the same kinetic energy spectrum slope of $k^{-4/3}$. They analyzed the energy transfer mechanisms in their simulations and argued that magnetic tension must be the dominant force for energy transfer across scales. The energy transfer mechanism in Kolmogorov turbulence, the kinetic energy cascade, is suppressed in this case by the magnetic tension, to which they attributed the cause of the shallower $k^{-4/3}$ energy spectrum. Although they believe that the bottleneck effect is not the cause of the $k^{-4/3}$ slope, their numerical resolution is still limited at (2048)³. The power-law slope measured in Grete et al. (2021) spans within ~ 2 dex of the dissipation scale, where the bottleneck effect is known to affect the energy spectrum (Ishihara et al. 2016). Moreover, there is no theoretical understanding so far about why the energy transfer by magnetic tension force may lead to the $k^{-4/3}$ energy spectrum. However, if the energy spectrum is indeed determined by the magnetic tension, the $k^{-4/3}$ slope can represent the inertial range of the turbulence cascade and extend to a much wider dynamic range far from the dissipation scale.

In addition, pure hydrodynamic instabilities can also generate turbulence in the protoplanetary disks in the absence of magnetic fields. For example, the subcritical baroclinic instability (SBI) driven by the radial entropy gradient (Klahr & Bodenheimer 2003; Klahr 2004; Petersen et al. 2007; Lesur & Papaloizou 2010) and the vertical shear instability (VSI) driven by the strong vertical shear (Nelson et al. 2013; Stoll & Kley 2016) can both generate long-lived turbulence in disks. Numerical simulations have found that the turbulence induced by the SBI or VSI can have much steeper kinetic energy spectra than the Kolmogorov turbulence across certain scales (Klahr & Bodenheimer 2003; Manger et al. 2020).

Given the uncertainty in the turbulence properties, this paper aims to provide insights into how non-Kolmogorov turbulence may affect grain collisional velocities and grain growth. In Section 2, we describe the turbulence models and the procedure for calculating the grain collisional velocities. We focus on three examples: the Kolmogorov turbulence, the IK turbulence, and the MRI turbulence described in Paper I. The results are shown in Section 3. Section 3.1 derives the analytic approximation for the collisional velocities assuming a general case of power-law turbulence spectrum, and Section 3.2 compares the analytic approximation with accurate numerical integration. We also supply publicly available Python scripts that implemented our formulae for calculating the collisional velocities. Section 3.3 shows the dependence of grain collisional velocity on turbulence parameters, by describing its behavior in different limiting regimes. Section 4.1 presents an application of our work: we calculate grain growth in protoplanetary disks with different turbulence models and estimate the fragmentation and drift barrier for grain growth due to non-Kolmogorov turbulence. Finally, Section 5 gives a summary of this work.

2. Method

We follow the method in Völk et al. (1980), Markiewicz et al. (1991), and OC2007 to calculate grain collisional velocities. These previous works considered only Kolmogorov turbulence. Here we generalize to a generic turbulence model with arbitrary

Table 1
Summary of Notations for the Key Physical Variables

Symbol	Meaning
\mathbf{v}	Gas velocity
$\delta\mathbf{v}$	$\mathbf{v} - \mathbf{v}_K$, turbulent gas velocity
v_{tot}	Large-scale turbulent velocity (Equation (5))
$v_{\text{rel}}(k)$	Relative velocity between grain and eddy (Equation (11))
$v_p \equiv \delta v_p$	Turbulence-induced grain velocity (Equation (8))
Δv_{12}	Collisional velocity between grains 1 and 2 (Equation (18))
St	Stokes number (Equation (9))
Re	Reynolds number (Equation (2))
τ_f	Grain friction/stopping time (Equation (8))
$\tau_{\text{cross}}(k)$	Eddy crossing time (Equation (13))
$\tau(k)$	Eddy autocorrelation time (Equation (7))
$E(k)$	Kinetic energy spectrum (Equation (1))
k_L	Injection scale (Figure 1)
k_η	Dissipation scale (Figure 1)
p	Power-law slope of $E(k)$
m	Power-law slope of $\tau(k)$

power-law slopes of energy spectrum and autocorrelation time. We first describe the turbulence model and then the steps to calculate the turbulence-induced grain collisional velocities. For the convenience of the reader, we summarize the important notations used in this paper in Table 1.

2.1. Turbulence Model

There are two important properties of turbulence that determine the grain collisional velocities: the kinetic energy spectrum $E(k)$ and the eddy autocorrelation time $\tau(k)$. We assume that the turbulence has a kinetic energy spectrum

$$E(k) = E_L \left(\frac{k}{k_L} \right)^{-p}, \quad k_L \leq k \leq k_\eta, \quad (1)$$

where k_L and k_η are the injection scale and dissipation scale of the turbulence. Outside of the range $k_L \leq k \leq k_\eta$, we simply assume $E(k) = 0$.³

The dissipation scale is determined by the Reynolds number,

$$Re = \frac{vL}{\nu}, \quad (2)$$

where ν is the viscosity, v is the velocity, and L is the length scale. Usually, the Reynolds number is defined for the largest turbulence eddy, $Re = Re(k_L) = v(k_L)L(k_L)/\nu$. For turbulence eddy k , $v(k) = \sqrt{kE(k)} \propto k^{(1-p)/2}$, and $L(k) \propto 1/k$. At the dissipation scale, $Re(k_\eta) = v(k_\eta)L(k_\eta)/\nu = 1$. This gives

$$Re = \frac{v(k_L)L(k_L)}{v(k_\eta)L(k_\eta)} = \left(\frac{k_\eta}{k_L} \right)^{(1+p)/2}, \quad (3)$$

or equivalently,

$$\frac{k_\eta}{k_L} = Re^{2/(1+p)}. \quad (4)$$

³ In Paper I, we found that the injection scale k_L is similar to the fastest-growing mode of the MRI in the disk, k_{MRI} . At $k < k_{\text{MRI}}$, there is still a region with $E(k) > 0$. However, because the slope of $E(k)$ in this region is much shallower than at $k > k_{\text{MRI}}$, the kinetic energy is dominated by $k \approx k_L$. Therefore, by using the simple assumption of $E(k) = 0$ for $k < k_L$, the dust collisional velocities are not affected significantly.

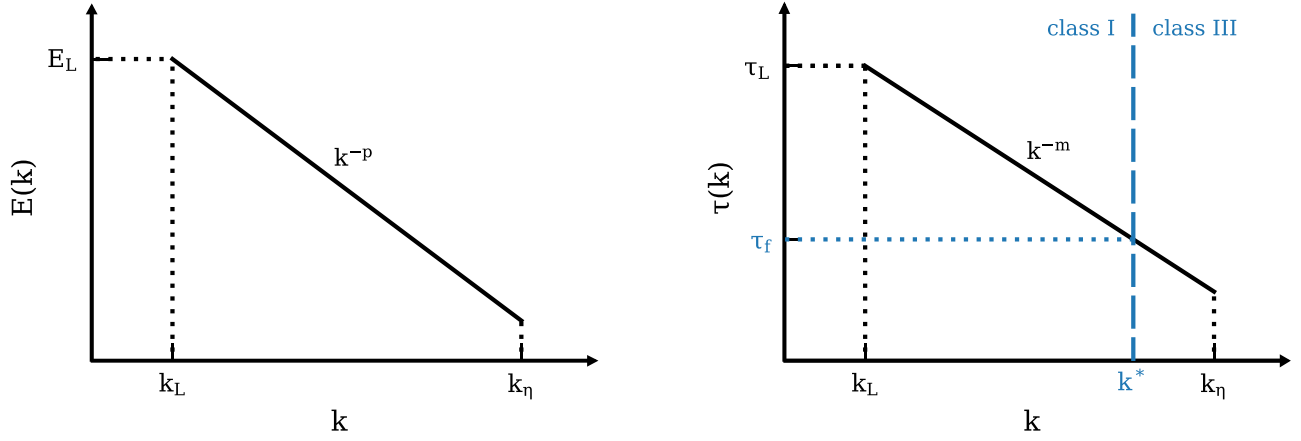


Figure 1. Schematic diagrams of the kinetic energy spectrum $E(k)$ (left panel) and the eddy autocorrelation time $\tau(k)$ (right panel). k_L and k_η denote the injection and dissipation scales, respectively. The blue annotations mark the transition between class I and class III eddies (see Equations (12)–(15)).

The large-scale (total) turbulent velocity v_{tot} is defined as

$$v_{\text{tot}}^2 = \int dk E(k). \quad (5)$$

From the Plancherel theorem, $v_{\text{tot}}^2 = \langle v^2 \rangle$, where v is the magnitude of turbulent gas velocity and “ $\langle \rangle$ ” denotes the spatial average. Integrating Equation (5), we have

$$v_{\text{tot}}^2 = \frac{E_L k_L}{p-1} \left[1 - \left(\frac{k_\eta}{k_L} \right)^{-(p-1)} \right] \approx \frac{E_L k_L}{p-1}. \quad (6)$$

For the integration to converge, it requires $p > 1$.

The corresponding turbulent autocorrelation time in the inertial range is

$$\tau(k) = \tau_L \left(\frac{k}{k_L} \right)^{-m}. \quad (7)$$

Figure 1 illustrates the models for $E(k)$ and $\tau(k)$. For the detailed definitions of $E(k)$ and $\tau(k)$ see Paper I.

Ormel & Cuzzi (2007) assumed $\tau(k) = 1/(k\sqrt{2kE(k)})$ from the kinetic cascade, which gives $\tau_L = 1/(k_L\sqrt{E_L k_L})$ and $m = (3-p)/2$. In Paper I, we did observe that $\tau(k) \approx 1/(k\sqrt{2kE(k)})$ for the MRI and driven turbulence.⁴ In principle, $\tau(k)$ can be influenced also by other physical processes such as the interaction between the gas and the magnetic field. Without losing generality, we keep p and m as separate parameters. We focus on three turbulence models shown in Table 2: the Kolmogorov turbulence, the IK turbulence, and the MRI turbulence in Paper I. We note that our method can also be applied to other turbulence models with arbitrary values of p and m .

2.2. Turbulence-induced Collisional Velocities

The dynamical property of a dust grain is characterized by its friction time (also often called the stopping time) τ_f . The randomly fluctuating component of grain velocity δv_p follows

⁴ In Paper I, we found that $\tau(k) \approx \min\{1/\Omega, 1/(k\sqrt{2kE(k)})\}$ for the MRI turbulence, where Ω is the local orbital frequency. With $k_{\text{MRI}} \approx \Omega/\langle v_{A,z} \rangle$, where $\langle v_{A,z} \rangle$ is the average Alfvén speed in the vertical direction, and $v_{\text{tot}} \approx \sqrt{E_L k_{\text{MRI}}} \approx \langle v_{A,z} \rangle$ (turbulent velocity comparable to the Alfvén speed), we have $(k_{\text{MRI}} \sqrt{2k_{\text{MRI}} E(k_{\text{MRI}})}) \approx \Omega$. This means $\tau(k) \approx 1/(k\sqrt{2kE(k)})$ at $k > k_{\text{MRI}}$.

Table 2
Parameters for Turbulence Models Considered in This Work

Model ^a	p	m	$(p-1)/m$
Kolmogorov	5/3	2/3	1
IK	3/2	3/4	2/3
Paper I	4/3	5/6	2/5

Note.

^a The parameter $(p-1)/m$ determines the scaling between the collisional velocity and the Stokes number for small grains (Equation (31)).

(Equation (5) in Völk et al. 1980)

$$\frac{d\delta v_p}{dt} = \frac{\delta v - \delta v_p}{\tau_f}, \quad (8)$$

where δv is the random component of the gas velocity, such as the turbulent velocity in the protoplanetary disk. For the simplicity of notations, we hereafter drop the δ in Equation (8) and use v_p to denote the randomly fluctuating component of grain velocity induced by turbulence.

It is convenient to define the dimensionless Stokes number

$$\text{St} = \tau_f / \tau_L. \quad (9)$$

Physically, τ_f or St is determined by the properties of both the grain and gas, as well as the relative velocity between them (Youdin 2010). For spherical grains in the Epstein drag regime (Epstein 1924), the friction time $\tau_f = \rho_s a / (\rho_g v_{\text{th}})$, where ρ_s and a are the material density and radius of the grain, ρ_g is the gas density, and v_{th} is the mean thermal velocity of the gas. In a protoplanetary disk, the Stokes number can be written as (Birnstiel et al. 2016)

$$\text{St} = \frac{\pi \rho_s a}{2 \Sigma_g}, \quad (10)$$

where Σ_g is the gas surface density. Using the minimum-mass solar nebula (MMSN) model in Hayashi (1981), $\text{St} \approx 10^{-8} - 1$ for typical grain sizes from 0.1 μm to 1 cm at 1–100 au.

In this work, only perturbations from the gas motions on dust grains are considered, and the back-reaction of dust grains onto the gas is ignored.

For two dust grains with friction times τ_{f1} and τ_{f2} , their collisional velocity Δv_{12} can be obtained by following the steps below:

1. Calculate the relative velocity $v_{\text{rel}}(k)$ between the eddy k and each dust grain (see Equation (19) in OC2007):

$$v_{\text{rel}}^2(k) = v_{\text{sys}}^2 + \int_{k_L}^k dk' E(k') \left(\frac{\tau_f}{\tau_f + \tau(k')} \right)^2, \quad (11)$$

where v_{sys} is the systematic velocity of the dust not driven by turbulence, such as the radial drift by pressure-gradient-driven headwind or vertical settling due to the stellar gravity. Throughout this work, we assume that the turbulent motions dominate and set $v_{\text{sys}} = 0$.

2. Determine the classes of eddies for each dust grain. The concept of “eddy classes” is first introduced by Völk et al. (1980). For a given dust grain with the friction time τ_f and a given eddy k , the eddy class is determined by

$$\begin{cases} \tau_f < \min\{\tau(k), \tau_{\text{cross}}(k)\}, & \text{class I eddy} \\ \tau_f \geq \min\{\tau(k), \tau_{\text{cross}}(k)\}, & \text{class III eddy,} \end{cases} \quad (12)$$

where

$$\tau_{\text{cross}}(k) = \frac{1}{kv_{\text{rel}}(k)} \quad (13)$$

is the timescale on which the grain moves across the eddy. Grains are well coupled with the class I eddies. This corresponds to small grains, for which τ_f is short enough that the grain “forgets” its initial motion and moves with the gas before it leaves the eddy or the eddy decays. On the contrary, grains are only weakly coupled with the class III eddies. Such grains are large enough that τ_f is long, and the eddy only exerts small perturbations to their motions. Because both $\tau(k)$ and $\tau_{\text{cross}}(k)$ increase with k , a grain is better coupled with the large eddies than the small eddies. The transition scale between class I and class III eddies is defined as k^* : the eddies are class I for $k < k^*$ and class III for $k \geq k^*$. k^* is a function of τ_f and can be solved by

$$\min\{\tau(k^*), \tau_{\text{cross}}(k^*)\} = \tau_f. \quad (14)$$

Appendix A shows that k^* can be approximated using $\tau(k) = \tau_f$. This gives

$$k^* = k_L \text{St}^{-1/m}. \quad (15)$$

Thus, there is no class I eddy for $\text{St} \geq 1$ and no class III eddy for $\text{St} \leq (k_L/k_\eta)^m$ (see the right panel of Figure 1).

3. Calculate the velocity dispersion of each dust grain. The velocity dispersion of a dust grain induced by turbulence is given by Equation (6) in Markiewicz et al. (1991),

$$v_p^2 = \int_I dk E(k)(1 - K^2) + \int_{\text{III}} dk E(k)(1 - K)[g(\chi) + Kh(\chi)], \quad (16)$$

where $K = \tau_f/[\tau_f + \tau(k)]$, $g(\chi) = \chi^{-1} \arctan(\chi)$, $h(\chi) = 1/(1 + \chi^2)$, and $\chi = K\tau(k)kv_{\text{rel}}(k)$. Here I and III denote the integration over class I ($k < k^*$) and class III ($k \geq k^*$) eddies, respectively.

4. Calculate the cross-correlation of the velocities between grains 1 and 2, $\langle v_{p1} \cdot v_{p2} \rangle$. From Equation (8) of

Markiewicz et al. (1991),

$$\begin{aligned} \langle v_{p1} \cdot v_{p2} \rangle &= \frac{1}{\tau_{f1} + \tau_{f2}} \int_{I_{12}} dk E(k) \\ &\times [\tau_{f1}(1 - K_1^2) + \tau_{f2}(1 - K_2^2)], \end{aligned} \quad (17)$$

where I_{12} denotes that the integration is over the eddies that are class I for both grains 1 and 2, i.e., $k < \min\{k_1^*, k_2^*\}$.

5. Obtain the collisional velocity between grains 1 and 2. Finally, the collisional velocity Δv_{12} can be calculated from

$$(\Delta v_{12})^2 = v_{p1}^2 + v_{p2}^2 - 2\langle v_{p1} \cdot v_{p2} \rangle. \quad (18)$$

For a given turbulence model, $(\Delta v_{12})^2$ is proportional to the total kinetic energy of the turbulence. Therefore, we usually present the normalized $\Delta v_{12}/v_{\text{tot}}$ in the following sections.

3. Results

3.1. Analytic Approximations for Grain Collisional Velocities

We calculate the analytic approximations of grain collisional velocities in different regimes. The k^* from Equation (15) is used to distinguish class I and class III eddies.

First, we calculate v_p^2 in Equation (16), which we divide into two terms, $v_p^2 = T_I + T_{\text{III}}$, where

$$T_I = \int_I dk E(k)(1 - K^2) \quad (19)$$

and

$$T_{\text{III}} = \int_{\text{III}} dk E(k)(1 - K)[g(\chi) + Kh(\chi)] \quad (20)$$

for the class I and class III eddies, respectively.

For the T_I term, there are two possible cases: (1) $\text{St} \geq 1$. There is no class I eddy, and $T_I = 0$. (2) $\text{St} < 1$. In this case, for class I eddies $\tau_f \leq \tau(k)$, and thus we can approximate $1 - K^2 \approx 1 - [\tau_f/\tau(k)]^2$. This gives

$$\begin{aligned} T_I(\text{St})|_{k_L}^{k'} &\approx \int_{k_L}^{k'} dk E(k) \left[1 - \left(\frac{\tau_f}{\tau(k)} \right)^2 \right] \\ &\approx v_{\text{tot}}^2 \left[1 - \left(\frac{k_L}{k'} \right)^{p-1} \right] \\ &\quad - \frac{p-1}{1+2m-p} \text{St}^2 v_{\text{tot}}^2 \left[\left(\frac{k'}{k_L} \right)^{1+2m-p} - 1 \right], \end{aligned} \quad (21)$$

where

$$k' = \min\{k^*, k_\eta\}. \quad (22)$$

$T_I(\text{St})|_{k_L}^{k'}$ denotes the integration of the function $E(k)(1 - K^2)$ in the range of $k_L \leq k \leq k'$ for a grain with Stokes number St .

For the T_{III} term, we use the approximation $g(\chi) \approx h(\chi) \approx 1$, following OC2007. This gives $(1 - K)[g(\chi) + Kh(\chi)] \approx 1 - K^2 \approx 2\tau(k)/\tau_f$, with $\tau(k) < \tau_f$ for class III eddies. There are

three cases: (1) $St \geq 1$. In this case, all eddies are class III, and

$$T_{III}(St)|_{k_L}^{k_\eta} \approx \int_{k_L}^{k_\eta} dk E(k) \frac{2\tau(k)}{\tau_f} \approx \frac{2(p-1)}{p+m-1} \frac{v_{tot}^2}{St} \left[1 - \left(\frac{k_L}{k_\eta} \right)^{p+m-1} \right]. \quad (23)$$

(2) $(k_L/k_\eta)^m < St < 1$. Class III eddies have $k > k^*$, and

$$T_{III}(St)|_{k^*}^{k_\eta} \approx \int_{k^*}^{k_\eta} dk E(k) \frac{2\tau(k)}{\tau_f} \approx \frac{2(p-1)}{p+m-1} \frac{v_{tot}^2}{St} \times \left[\left(\frac{k_L}{k^*} \right)^{p+m-1} - \left(\frac{k_L}{k_\eta} \right)^{p+m-1} \right]. \quad (24)$$

(3) $St \leq (k_L/k_\eta)^m$. There are no class III eddies, and $T_{III} = 0$.

The cross-correlation term in Equation (17) is only nonzero for two grains with $St_1 < 1$ and $St_2 < 1$. Assuming $St_2 < St_1 < 1$, Equation (17) can be written as

$$\langle v_{p1} \cdot v_{p2} \rangle = \frac{St_1}{St_1 + St_2} T_I(St_1)|_{k_L}^{k_1'} + \frac{St_2}{St_1 + St_2} T_I(St_2)|_{k_L}^{k_2'}, \quad (25)$$

where $k_1' = \min\{k_1^*, k_\eta\}$. The analytic approximation can be obtained from Equation (21).

3.2. Comparisons with Numerical Integrations

The collisional velocities Δv_{12} between two dust grains with Stokes numbers St_1 and St_2 in different turbulence models are shown in Figure 2, with Reynolds number $Re = 10^8$. The top panels show the collisional velocity from numerical integrations. In the regions where $St_1 \geq 1$ or $St_2 \geq 1$, the collisional velocities are very similar across different turbulence models. However, in the regions where $St_1, St_2 < 1$, the collisional velocities can differ by orders of magnitude depending on the turbulence model. This behavior is explained in Section 3.3, where we derive the scaling relationship between Δv_{12} and turbulence parameters.

The analytic approximation of Δv_{12} is shown in the middle panels of Figure 2, and the differences between the analytic approximation and numerical integration are shown in the bottom panels. The analytic approximation is accurate within 30% in most regions and within 70% in all regions. The largest error occurs close to $St = 1$, $St_1 = St_2$, and $St = (k_L/k_\eta)^m$, where the criteria for analytic approximations are not satisfied (see Section 3.1).

The analytic approximation allows for fast and accurate calculation of grain collisional velocities with arbitrary turbulence properties, without significant sacrifice in the accuracy. The analytic formulae in Section 3.1 can be easily implemented in grain growth codes, enabling the calculation of grain size evolution in non-Kolmogorov turbulence. We provide publicly available Python scripts that implemented our calculations at https://github.com/munan/grain_collision.

3.3. Limiting Behaviors

In order to obtain a clear physical understanding of the dependence of grain collisional velocities Δv_{12} on the

turbulence properties in Figure 2, we discuss the limiting behaviors of Δv_{12} . We divide the Stokes numbers St_1 and St_2 into four regimes and discuss the dependence of Δv_{12} on turbulence parameters in each regime. Figure 3 summarizes the limiting behaviors of Δv_{12} . Here we call the grains “big”, “small,” or “tiny” defined by their Stokes numbers, which determine the scales of the turbulence eddies that they are coupled with. We always assume that the Reynolds number is large, and therefore $k_L/k_\eta \rightarrow 0$.

3.3.1. Two Big Grains

Take two big grains with $St_1 > 1$ and $St_2 > 1$: the eddies are all class III, and the cross term in Equation (17) vanishes. We can use Equation (23) to obtain

$$\begin{aligned} (\Delta v_{12})^2 &= v_{p1}^2 + v_{p2}^2 \\ &= T_{III}(St_1)|_{k_L}^{k_\eta} + T_{III}(St_2)|_{k_L}^{k_\eta} \\ &\approx \frac{2(p-1)v_{tot}^2}{p+m-1} \left[1 - \left(\frac{k_L}{k_\eta} \right)^{p+m-1} \right] \left(\frac{1}{St_1} + \frac{1}{St_2} \right) \\ &\approx v_{tot}^2 \left(\frac{1}{St_1} + \frac{1}{St_2} \right). \end{aligned} \quad (26)$$

The last step uses the approximation that the factor $2(p-1)/(p+m-1)$ is of order unity, and $k_L/k_\eta \ll 1$. In this case, each of the two grains is moving at an uncorrelated velocity of $v_p \approx v_{tot}/\sqrt{St}$. The velocity perturbation is dominated by the largest eddy.

3.3.2. One Big Grain and One Small Grain

Take one big grain with $St_1 > 1$ and one small grain with $St_2 < 1$: from Equations (19) and (20) we have

$$\begin{aligned} (\Delta v_{12})^2 &= v_{p1}^2 + v_{p2}^2 \\ &= T_{III}(St_1)|_{k_L}^{k_\eta} + T_I(St_2)|_{k_L}^{k_2'} + T_{III}(St_2)|_{k_2'}^{k_\eta}, \end{aligned} \quad (27)$$

where $k_2' = \min\{k_2^*, k_\eta\}$. In the limit of $St_1 \rightarrow \infty$ and $St_2 \rightarrow 0$, the terms $T_{III}(St_1)|_{k_L}^{k_\eta}$ and $T_{III}(St_2)|_{k_2'}^{k_\eta}$ vanish. Following Equation (21),

$$(\Delta v_{12})^2 \approx T_I(St_2)|_{k_L}^{k_2'} \approx v_{tot}^2. \quad (28)$$

The bigger grain 1 barely moves owing to its large mass, and the smaller grain 2 is well coupled with the gas and moves at the turbulent velocity v_{tot} .

3.3.3. Two Small Grains

Take two small grains with $(k_L/k_\eta)^m < St_1 < 1$ and $St_2 < St_1$, we have

$$\begin{aligned} (\Delta v_{12})^2 &= v_{p1}^2 + v_{p2}^2 - 2\langle v_{p1} \cdot v_{p2} \rangle \\ &= T_I(St_1)|_{k_L}^{k_1^*} + T_{III}(St_1)|_{k_1^*}^{k_\eta} + T_I(St_2)|_{k_L}^{k_2'} \\ &\quad + T_{III}(St_2)|_{k_2'}^{k_\eta} - 2 \frac{St_1}{St_1 + St_2} T_I(St_1)|_{k_L}^{k_1^*} \\ &\quad - 2 \frac{St_2}{St_1 + St_2} T_I(St_2)|_{k_L}^{k_2'}. \end{aligned} \quad (29)$$

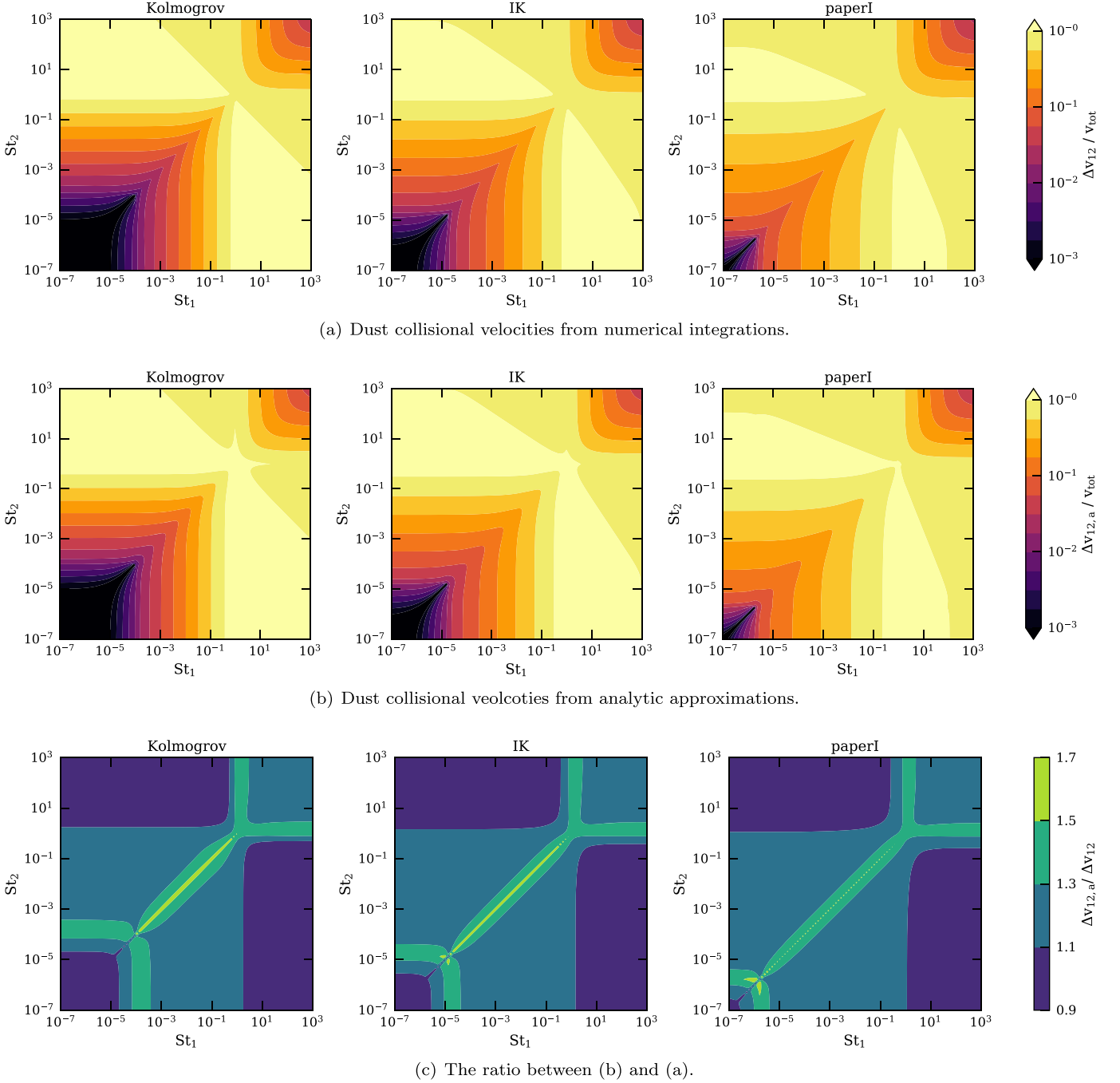


Figure 2. Collisional velocities Δv_{12} between two dust grains with Stokes numbers St_1 and St_2 , normalized by the total gas turbulent velocity v_{tot} , in Kolmogorov (left), IK (middle), and Paper I (right) turbulence models. (a) Collisional velocity Δv_{12} from direct numerical integrations. (b) Collisional velocity $\Delta v_{12,a}$ from analytic approximations. (c) The ratio $\Delta v_{12,a} / \Delta v_{12}$.

We split the term $T_I(St_2)|_{k_L}^{k_2'}$ into two components, $T_I(St_2)|_{k_L}^{k_1^*} + T_I(St_2)|_{k_1^*}^{k_2'}$, and neglect the second one compared to the first one, which allows us to approximate $T_I(St_2)|_{k_L}^{k_2'} \approx T_I(St_2)|_{k_L}^{k_1^*}$. In addition, one can easily show that $T_{\text{III}}(St_2)|_{k_2'}^{k_\eta} < T_{\text{III}}(St_1)|_{k_1^*}^{k_\eta}$, and therefore the former term can be ignored. With these approximations, we write

$$\begin{aligned}
 (\Delta v_{12})^2 &\approx \frac{St_1 - St_2}{St_1 + St_2} [T_I(St_2) - T_I(St_1)]|_{k_L}^{k_1^*} + T_{\text{III}}(St_1)|_{k_1^*}^{k_\eta} \\
 &\approx \frac{(p-1)(St_1 - St_2)^2 v_{\text{tot}}^2}{1 + 2m - p} \left[\left(\frac{k_1^*}{k_L} \right)^{1+2m-p} - 1 \right] \\
 &\quad + \frac{2(p-1)v_{\text{tot}}^2}{(p+m-1)St_1} \left(\frac{k_L}{k_1^*} \right)^{p+m-1}. \quad (30)
 \end{aligned}$$

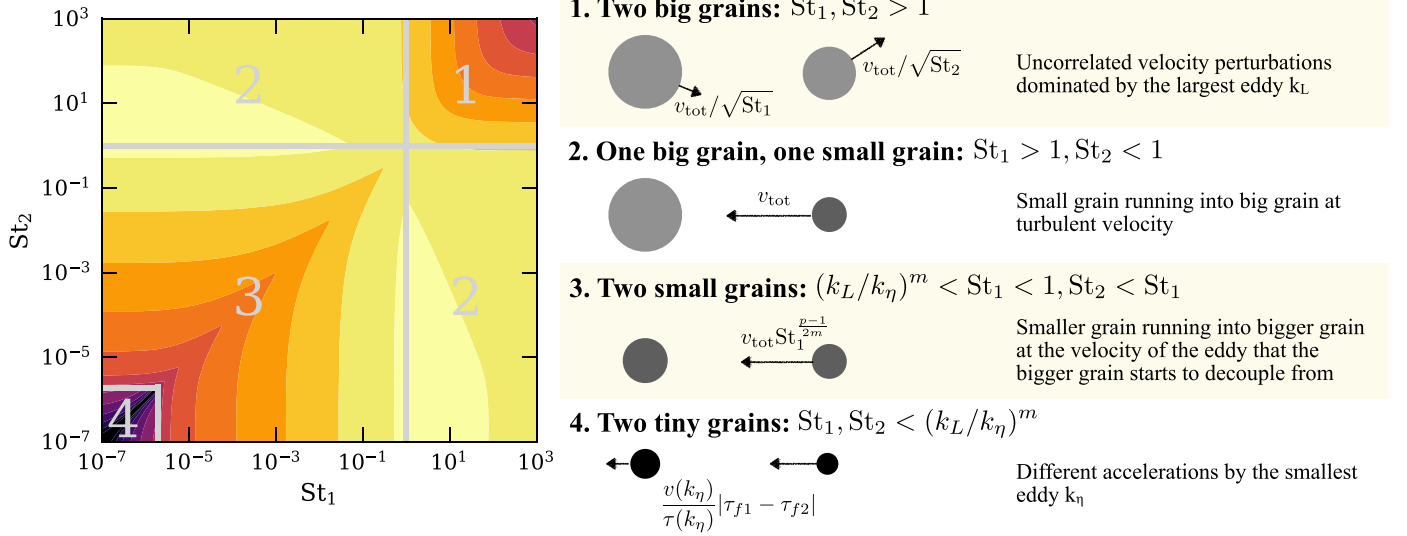


Figure 3. The limiting behaviors of the grain collisional velocity Δv_{12} in different regimes of the Stokes numbers. In regimes 1 and 2, Δv_{12} is dominated by the total turbulent velocity and is insensitive to the turbulence properties. In regimes 3 and 4, Δv_{12} depends sensitively on the turbulence properties. The transition boundary between the two regimes and the grain collisional velocities are sensitive to the Reynolds number Re , the power-law slope of the turbulence energy spectrum p , and the power-law slope of the turbulence autocorrelation time m .

If we take the limit of $St_2 \ll St_1 \ll 1$, then $k_1^*/k_L = St_1^{-1/m} \gg 1$, giving

$$(\Delta v_{12})^2 \approx v_{\text{tot}}^2 St_1^{(p-1)/m}. \quad (31)$$

We can understand this scaling relation by considering the coupling of the dust grains with the gas: for eddies $k < k_1^*$, both grains are well coupled with the gas, and the relative velocities are small. The collisional velocity is therefore dominated by the eddy k_1^* , where the larger grain 1 starts to decouple with the gas and the smaller grain 2 is still well coupled with the gas, running into the larger grain at the eddy velocity. The velocity of the eddy k_1^* is

$$v^2(k_1^*) \sim k_1^* E(k_1^*) \sim v_{\text{tot}}^2 St_1^{(p-1)/m}. \quad (32)$$

Here the slope of the autocorrelation time m determines the scale at which the larger grain starts to decouple, and the slope of the energy spectrum p determines the eddy velocity at that scale.

3.3.4. Two Tiny Grains

Take two tiny grains with $St_1, St_2 < (k_L/k_\eta)^m$, and assuming $St_2 < St_1$, all eddies are class I. Similar to Equation (30),

$$\begin{aligned} (\Delta v_{12})^2 &\approx \frac{St_1 - St_2}{St_1 + St_2} [T_I(St_2) - T_I(St_1)]|_{k_L}^{k_\eta} \\ &\approx v_{\text{tot}}^2 \left(\frac{k_\eta}{k_L} \right)^{1+2m-p} (St_1 - St_2)^2 \\ &\approx \left[\frac{v(k_\eta)}{\tau(k_\eta)} (\tau_{f1} - \tau_{f2}) \right]^2. \end{aligned} \quad (33)$$

The collisional velocity is dominated by the smallest eddy k_η . The two grains of different sizes accelerate at different rates, causing the relative velocity. For grains with the exact same size, the collisional velocity is zero. The collisional velocity depends on the dissipation scale k_η , as well as the velocity and

autocorrelation time of the eddy k_η . These are in turn determined by the Reynolds number, the energy spectrum slope p , and the slope of the autocorrelation time m .

4. Applications to Protoplanetary Disks

4.1. Grain Size Evolution

Turbulence plays a crucial role in grain evolution in protoplanetary disks. It provides the dominant source of collisional velocities for micron- to centimeter-sized grains, which are too large to coagulate efficiently, due to Brownian motion, and too small to experience strong differential radial and azimuthal drift (Testi et al. 2014).

To show the impact of turbulence properties on grain evolution, we perform numerical simulations of grain coagulation in typical disk environments, similar to Akimkin et al. (2020b). We consider the simplest case of noncharged compact spherical grains with a material density of $\rho_s = 3.0 \text{ g cm}^{-3}$, a fixed dust-to-gas ratio of $\rho_d/\rho_g = 0.01$, and a constant turbulence alpha-parameter of $\alpha = 10^{-4}$. This low value of α is motivated by recent constraints by both dust and gas observations (Pinte et al. 2016; Flaherty et al. 2018), as well as from theoretical models (Simon et al. 2018). We take two sets of physical conditions in the disk: (1) $\rho_g = 5 \times 10^{-14} \text{ g cm}^{-3}$, $T_g = 38 \text{ K}$, and (2) $\rho_g = 3 \times 10^{-15} \text{ g cm}^{-3}$, $T_g = 25 \text{ K}$, where ρ_g and T_g are the gas density and temperature, respectively. These correspond to the conditions in the disk midplane at 30 and 70 au in Akimkin et al. (2020b). We choose to focus on the outer disk for the following reasons: (1) it is better probed by observations with its larger spatial scales and longer evolution timescales, and (2) the grain growth is less affected by fragmentation and radial drift, which we do not include in our model. In fact, for the parameter we choose, the maximum grain collisional velocity is $v_{\text{coll}} \approx v_{\text{tot}} \approx 4 \text{ m s}^{-1}$, smaller than the typical fragmentation velocity of $\sim 10 \text{ m s}^{-1}$ (Gundlach & Blum 2015). Using Equation (40) in Section 4.3, we calculated that the radial drift barrier occurs for grains of sizes $\approx 5 \text{ mm}$ at 30 au and $\approx 0.4 \text{ mm}$ at 70 au (marked by the filled circles in Figure 5). However, we note

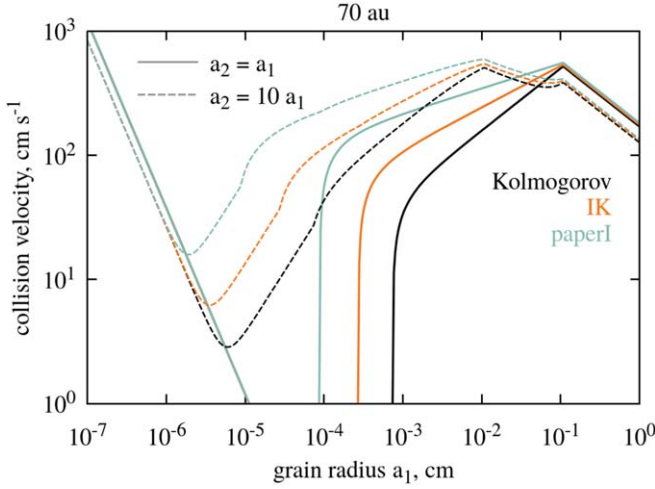


Figure 4. Illustration of collision velocities between equal-size grains (solid lines) and grains with an order-of-magnitude size disparity (dashed lines). The results are for our three turbulence models (Kolmogorov, IK, and Paper I) at 70 au. For very small grains, the collisional velocity is dominated by the Brownian motion, which scales as $a^{-3/2}$. For larger grains, the collisional velocity is determined by turbulence and can be approximately described by the four regimes discussed in Section 3.3. Consecutive transitions between regimes 4 and 1 (see Figure 3) are evident following the dashed lines ($a_2 = 10a_1$) as a_1 increases. For a wide range of grain sizes from submicron to millimeter, the collisional velocity is very sensitive to the turbulence properties.

that the radial drift is very sensitive to the disk structure commonly observed (Andrews 2020; Segura-Cox et al. 2020). Nonsmooth structures such as gaps and rings in the disk will significantly deter the drift.

The initial grain size distribution is taken to be a power law with a slope of -3.5 in the range of $0.005\text{--}0.25\text{ }\mu\text{m}$ (Mathis et al. 1977). The coagulation equation is solved on a grid of grain masses ranging from 10^{-20} to 10^7 g (roughly corresponding to sizes from 10^{-7} to 10^2 cm) with 512 bins, providing resolution of ~ 20 bins per grain mass decade or ~ 60 bins per grain size decade.

We consider two sources of grain collisional velocities: the Brownian motion Δv_{Br} and turbulence-induced velocities Δv_{12} . The total grain collisional velocity is $\Delta v_{\text{coll}} = \sqrt{(\Delta v_{\text{Br}})^2 + (\Delta v_{12})^2}$. In Figure 4 we show the collisional velocities between equal-size grains and grains with an order of size disparity, calculated at 70 au. The Brownian motion with $\Delta v_{\text{Br}} \propto a^{-3/2}$ dominates for the smallest sizes. For a near the transition to turbulence-driven motion, the resulting collision velocity exhibits a deep minimum, naturally leading to a slower coagulation for these sizes. This explains the small bump seen for micron-size grains in the size distribution (see the left panel of Figure 6 in Appendix B). For a large range of grain sizes from submicron to millimeter, the collisional velocity is very sensitive to the turbulence model, leading to dramatically different growth rates. To demonstrate the observational effect of different turbulence models on grain size evolution, we calculate the dust opacity coefficient $\kappa_\nu(t) = \int \pi a^2 Q_{\text{abs}}(a, \nu) f(m, t) dm / \rho_d$, where $f(m, t)$ is the grain mass distribution, $\rho_d = \int m f(m, t) dm$, and $Q_{\text{abs}}(a, \nu)$ is the absorption efficiency obtained using the Mie theory for spherical silicate grains (Draine & Lee 1984; Akimkin et al. 2020a).

The left panels of Figure 5 show the evolution of the average grain radius for the three cases of turbulence models (Kolmogorov, IK, and Paper I). The average grain radius $\bar{a}(t)$ is calculated from

$$\frac{4\pi}{3} \rho_s \bar{a}^3(t) = \frac{\int m^2 f(m, t) dm}{\rho_d}. \quad (34)$$

The corresponding dust opacity at the wavelength of 1.3 mm (ALMA Band 6) is illustrated in the right panels of Figure 5. The evolution of grain size distribution and dust opacity at 70 au is presented in Figure 6 in Appendix B. The evolution at 30 au is qualitatively similar to that at 70 au but occurs faster owing to the higher density and turbulent velocity. The higher collisional velocity for smaller grains in the IK and Paper I turbulence makes their growth faster than in the standard Kolmogorov turbulence case. The size range of $0.1\text{--}0.5\text{ mm}$ (gray shaded region in the left panels of Figure 5) is important, as such grains contribute the most to the disk millimeter emission (Rosotti et al. 2019; Akimkin et al. 2020a). This is also shown in the right panels of Figure 5: as the average grain size increases, the 1.3 mm dust opacity first increases and then decreases, peaking around the $0.1\text{--}0.5\text{ mm}$ size range. At 70 au, the grains grow to submillimeter sizes within 0.1 Myr with the Paper I turbulence, while for the Kolmogorov turbulence it takes 1 Myr to reach the same sizes.

The faster grain growth enabled by the non-Kolmogorov turbulence has interesting implications in many observational and theoretical aspects. This can result in rapid radial drift of dust grains in the outer disk, leading to the small disk sizes observed in class 0 and I protostars (Segura-Cox et al. 2016, 2018). Furthermore, it is known that grain charging may completely stop coagulation for micron-sized grains, especially for fluffy aggregates (Okuzumi 2009; Akimkin et al. 2020b). The higher collisional velocities provided by the IK and Paper I turbulence can help to overcome this charge barrier. Generally, the faster grain growth provides more favorable conditions for early planet formation in young disks, by both accelerating the core formation processes and supplying solid material from the outer disk by the radial drift.

4.2. Fragmentation Barrier

We calculate the fragmentation barrier for grain growth following Birnstiel et al. (2012), but we take into account the dependence of grain collisional velocities on turbulence properties. We estimate the collisional velocities of dust grains with $\text{St} < 1$ from Equation (31),

$$\Delta v_{\text{coll}} \approx \sqrt{\alpha} c_s \text{St}^{\frac{p-1}{2m}}, \quad (35)$$

where c_s is the sound speed. By equating Δv_{coll} to the fragmentation velocity v_{frag} , we obtain the fragmentation barrier site,

$$a_{\text{frag}} = \frac{\pi \Sigma_g}{2 \rho_s} \left[\frac{1}{\alpha} \left(\frac{v_{\text{frag}}}{c_s} \right)^2 \right]^{\frac{m}{p-1}}. \quad (36)$$

For Kolmogorov turbulence, where $m/(p-1) = 1$, we recover Equation (8) in Birnstiel et al. (2012) within a pre-factor of order unity. For both the IK and Paper I turbulence, the higher collisional velocities lead to smaller values of a_{frag} than that for the Kolmogorov turbulence. We note that the largest collisional velocity occurs for grains with $\text{St} \approx 1$ (see Section 3.3) at $\Delta v_{\text{coll}} \approx \sqrt{\alpha} c_s$. If $\sqrt{\alpha} c_s < v_{\text{frag}}$, the fragmentation barrier is never reached (which is true for the cases considered in Section 4.1).

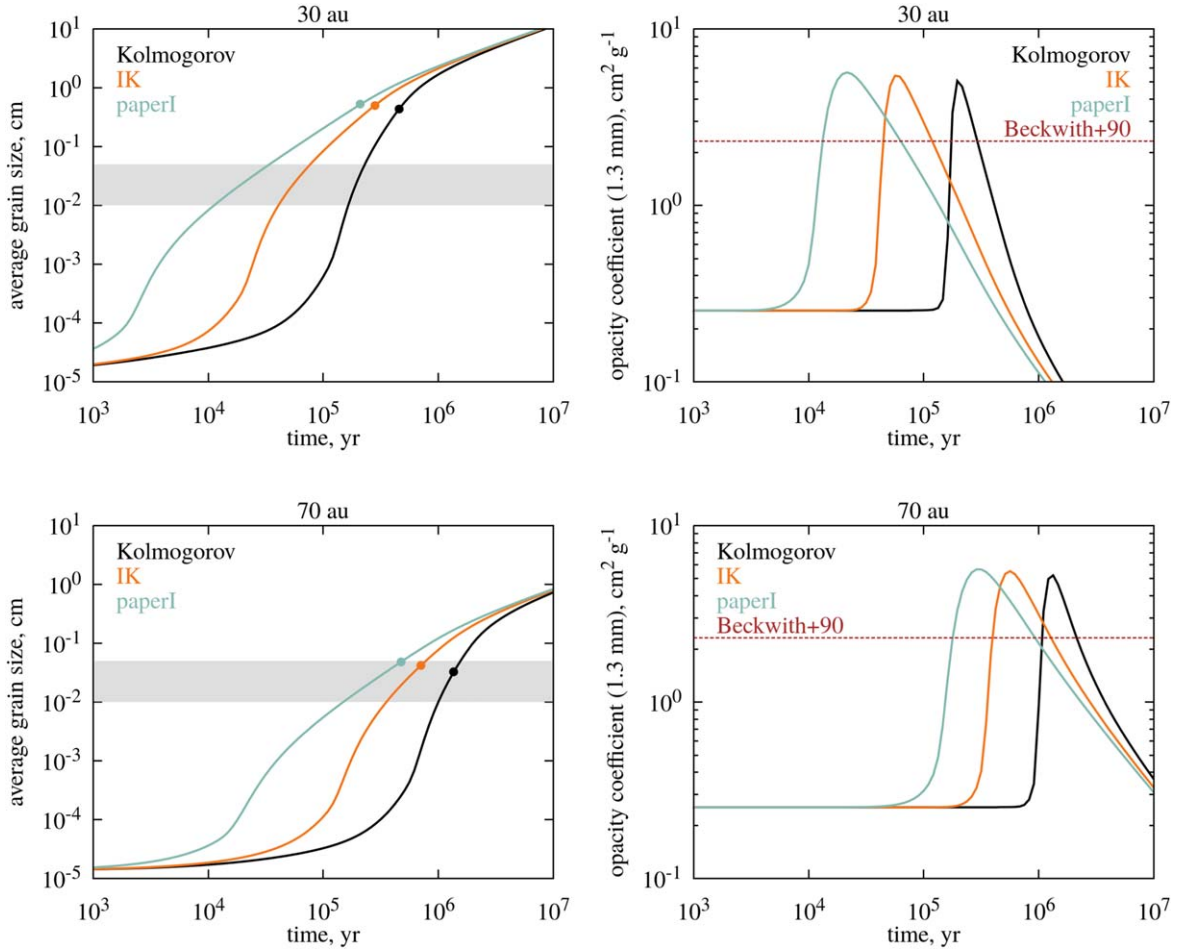


Figure 5. Left: evolution of the average grain size (Equation (34)) in the disk midplane at 30 and 70 au. The gray shaded region marks the size range that contributes the most to the dust emission at millimeter wavelengths. The filled circles indicate radial drift barriers for each turbulence model according to Equation (40). Right: evolution of the dust opacity coefficient at the wavelength $\lambda = 1.3$ mm (ALMA Band 6). The horizontal red dashed line shows the opacity coefficient of $2.3 \text{ cm}^2 \text{ g}^{-1}$ in the observations by Beckwith et al. (1990).

4.3. Radial Drift Barrier

Similar to the fragmentation barrier, the radial drift barrier also depends on the turbulence properties, which influences the grain growth timescale. From Birnstiel et al. (2012), the grain growth timescale is

$$\tau_{\text{grow}} = \frac{a\rho_s}{\rho_d \Delta v_{\text{coll}}}, \quad (37)$$

with the collisional velocity from Equation (35). The dust density ρ_d is obtained from $\rho_d = \Sigma_d / (\sqrt{2\pi} h_d)$, where the dust surface density is given by $\Sigma_d = \epsilon \Sigma_g$ with a constant dust-to-gas ratio $\epsilon = 0.01$. The dust disk scale height h_d is calculated by Youdin & Lithwick (2007),

$$h_d = \sqrt{\frac{\alpha}{\text{St}}} h_g, \quad (38)$$

where h_g is the gas disk scale height.⁵ The drift timescale is

⁵ The dust disk scale height in Equation (38) is obtained from the balance of vertical settling and turbulent diffusion of dust grains. Turbulent diffusion is dominated by the largest eddy and not sensitive to the detailed energy spectrum (Youdin & Lithwick 2007). Therefore, Equation (38) can be applied to all three turbulence models considered in this work.

$$\tau_{\text{drift}} = \frac{rv_k}{\gamma \text{St} c_s^2}, \quad (39)$$

where r is the disk radius and $\gamma = |d \ln P / d \ln r|$ is the absolute value of the power-law index of the gas pressure profile in the disk. From $\tau_{\text{grow}} = \tau_{\text{drift}}$, we obtain the drift barrier site,

$$a_{\text{drift}} = \frac{2}{\pi} \frac{\Sigma_g}{\rho_s} \left[\left(\frac{\pi}{8} \right)^{1/2} \frac{\epsilon}{\gamma} \left(\frac{h_g}{r} \right)^{-2} \right]^{\frac{2m}{3m-p+1}}. \quad (40)$$

For Kolmogorov turbulence,

$$a_{\text{drift,Kol}} = \frac{1}{\sqrt{2\pi}} \frac{\Sigma_d}{\rho_s \gamma} \left(\frac{h_g}{r} \right)^{-2}, \quad (41)$$

which recovers the result from Equation (33) in Birnstiel et al. (2016). The values of a_{drift} are higher for the IK and Paper I turbulence compared to that for the Kolmogorov turbulence, due to the higher collisional velocities and faster grain growth rates (Figure 5).

5. Summary

In this paper, we calculate grain collisional velocities for an arbitrary turbulence model characterized by three dimensionless parameters: the slope of the kinetic energy spectrum p , the slope of

the autocorrelation time m , and the Reynolds number Re . Our work is a significant extension of calculations by OC2007, which, although being widely adopted in the literature, are only applicable to the Kolmogorov turbulence. As an example, we focus on three different turbulence models: the standard Kolmogorov turbulence, the IK model of MHD turbulence, and the MRI turbulence described in Paper I. We calculate the grain collisional velocities using numerical integration. In addition, we derive accurate analytic approximations of the collisional velocities and give scaling relations with the Stokes numbers and turbulence properties. To demonstrate the implications, we perform numerical simulations of the grain size evolution in the outer regions of protoplanetary disks and calculate the fragmentation and radial drift barrier for grain growth in non-Kolmogorov turbulence models. The main findings of this paper are summarized as follows:

1. We calculate the grain collisional velocities between two dust grains in different turbulence models using both numerical integration and analytic approximations (Figure 2). The analytic approximation is simple and accurate and can be readily implemented in complex numerical codes to model the grain size evolution in arbitrary turbulence models. We provide publicly available Python scripts implementing our calculations at https://github.com/munan/grain_collision.
2. We introduce four characteristic regimes for the collisional velocities, depending on the Stokes numbers of the grains. We perform a detailed analysis of each regime, revealing the dominant mechanism that governs the collisional velocities and presenting the corresponding scaling relations (Figure 3). In particular, we show that the collisional velocities of small grains with $St < 1$ depend sensitively on the turbulence properties, with $(\Delta v_{12})^2 \sim St^{(p-1)/m}$ (Equation (31)).
3. The collisional velocities of small grains in IK and Paper I turbulence are much higher (more than an order of magnitude for some grain sizes) than that in the Kolmogorov turbulence (Figure 4).
4. We perform numerical simulations of grain size evolution in the outer parts of protoplanetary disks. Compared to the Kolmogorov turbulence, the higher grain collisional velocities lead to faster grain growth in the IK and Paper I turbulence models (Figure 5). For the MRI turbulence in Paper I, grains can grow to submillimeter sizes within ~ 0.1 Myr even with a very low turbulence level ($\alpha = 10^{-4}$) at 70 au. For Kolmogorov turbulence, growth to such sizes takes ~ 1 Myr.
5. The faster grain growth in the IK and Paper I turbulence may lead to rapid increase of dust opacity at millimeter wavelength (Figure 5). Increased collisional velocities can also help to overcome the charge barrier for the coagulation of micron-sized dust grains, accelerate the growth of pebbles and planetesimals, and thus promote planet formation in very young disks.
6. We calculate the fragmentation and drift barriers for grain growth in non-Kolmogorov turbulence (Equations (36) and (40)). Compared to the Kolmogorov turbulence, the higher grain collisional velocities for the IK and Paper I turbulence lead to smaller values of a_{frag} and larger values of a_{drift} .

In the future, our calculations can be implemented in numerical codes to explore the effect of non-Kolmogorov turbulence on the grain size evolution in a wide range of environments.

M. Gong, A. Ivlev, and P. Caselli acknowledge the support of the Max-Planck Society. M. Gong thanks Hubert Klahr for helpful discussions on this work. V. Akimkin acknowledges the support of the Ministry of Science and Higher Education of the Russian Federation under grant 075-15-2020-780 (N13.1902.21.0039).

Appendix A Eddy Class

The eddy classes in Equation (12) are determined by both the autocorrelation time $\tau(k) = 1/(kv_{\text{vel}}(k))$ and the eddy crossing time $\tau_{\text{cross}}(k) = 1/(kv_{\text{vel}}(k))$. Below we show that $v(k) \gtrsim v_{\text{rel}}(k)$ for class I eddies, and hence $\tau(k) \lesssim \tau_{\text{cross}}(k)$ in this case. Therefore, the transition scale k^* can be calculated from the condition $\tau(k) = \tau_f$. There are three scenarios:

1. $St \geq 1$. In this case $\tau_f > \tau_L$, and all eddies are class III.
2. $(k_\eta/k_L)^{-m} < St < 1$. We define k_f to be the scale where $\tau(k_f) = \tau_f$, and thus $k_f/k_L = St^{-1/m}$. Below we obtain that $v_{\text{rel}}(k)$ is an increasing function of k for $k \leq k_f$, whereas $\tau(k)$ always decreases with k . Therefore, for our purposes it is sufficient to show that $v(k_f) \gtrsim v_{\text{rel}}(k_f)$. Because $\tau(k) \geq \tau_f$ at $k \leq k_f$, we can approximate $v_{\text{rel}}(k)$ in Equation (11) with

$$\begin{aligned} v_{\text{rel}}^2(k_f) &\approx \int_{k_L}^{k_f} dk E(k) \left(\frac{\tau_f}{\tau(k)} \right)^2 \\ &= k_L E_L St^2 \int_1^{k_f/k_L} x^{2m-p} dx \\ &\approx \frac{p-1}{2m+1-p} v_{\text{tot}}^2 St^2 \left(\frac{k_f}{k_L} \right)^{2m+1-p} \\ &= \frac{p-1}{2m+1-p} v_{\text{tot}}^2 St^{(p-1)/m}. \end{aligned} \quad (\text{A1})$$

To approximate the integration, the second-to-last step used the fact that $2m+1-p > 1$ for the turbulence models we considered (Table 2), as well as $k_f/k_L > 1$. For $v(k)$, we have

$$\begin{aligned} v^2(k_f) &= 2k_f E(k_f) = 2k_L E_L \left(\frac{k_f}{k_L} \right)^{1-p} \\ &= 2(p-1) v_{\text{tot}}^2 St^{(p-1)/m}. \end{aligned} \quad (\text{A2})$$

Comparing Equations (A1) and (A2), we obtain $v(k_f) \gtrsim v_{\text{rel}}(k_f)$, and thus $\tau(k_f) \lesssim \tau_{\text{cross}}(k_f)$. This gives $k^* \approx k_f$ and thus

$$k^* \approx k_L St^{-1/m}. \quad (\text{A3})$$

3. $St \leq (k_\eta/k_L)^{-m}$. In this last case, we compare $v_{\text{rel}}(k_\eta)$ to $v(k_\eta)$. From Equation (A1), we have

$$\begin{aligned} v_{\text{rel}}^2(k_\eta) &\approx \frac{1}{2m+1-p} k_L E_L St^2 \left(\frac{k_\eta}{k_L} \right)^{2m+1-p} \\ &\leq \frac{p-1}{2m+1-p} v_{\text{tot}}^2 \left(\frac{k_\eta}{k_L} \right)^{-(p-1)}, \end{aligned} \quad (\text{A4})$$

and similar to Equation (A2),

$$v^2(k_\eta) = 2(p-1) v_{\text{tot}}^2 \left(\frac{k_\eta}{k_L} \right)^{-(p-1)}. \quad (\text{A5})$$

This gives $v(k_\eta) \gtrsim v_{\text{rel}}(k_\eta)$ and $\tau(k_\eta) \lesssim \tau_{\text{cross}}(k_\eta)$, similar to the previous case. In this case, all eddies are class I.

Appendix B

Grain Size Distribution and Opacity Coefficients

Figure 6 shows the evolution of the grain size distribution and wavelength-dependent dust opacity coefficients at 70 au

for the Kolmogorov, IK, and Paper I turbulence models. The early evolution at $t \lesssim 10^4$ yr is governed by the Brownian motion and therefore insensitive to the turbulence properties. Higher turbulence-induced collisional velocities in the Paper I case (see Figure 4) push the peak of the grain size distribution to $\sim 100 \mu\text{m}$ already at 10^5 yr, giving rise to an earlier increase of dust opacities in the millimeter wavelength range.

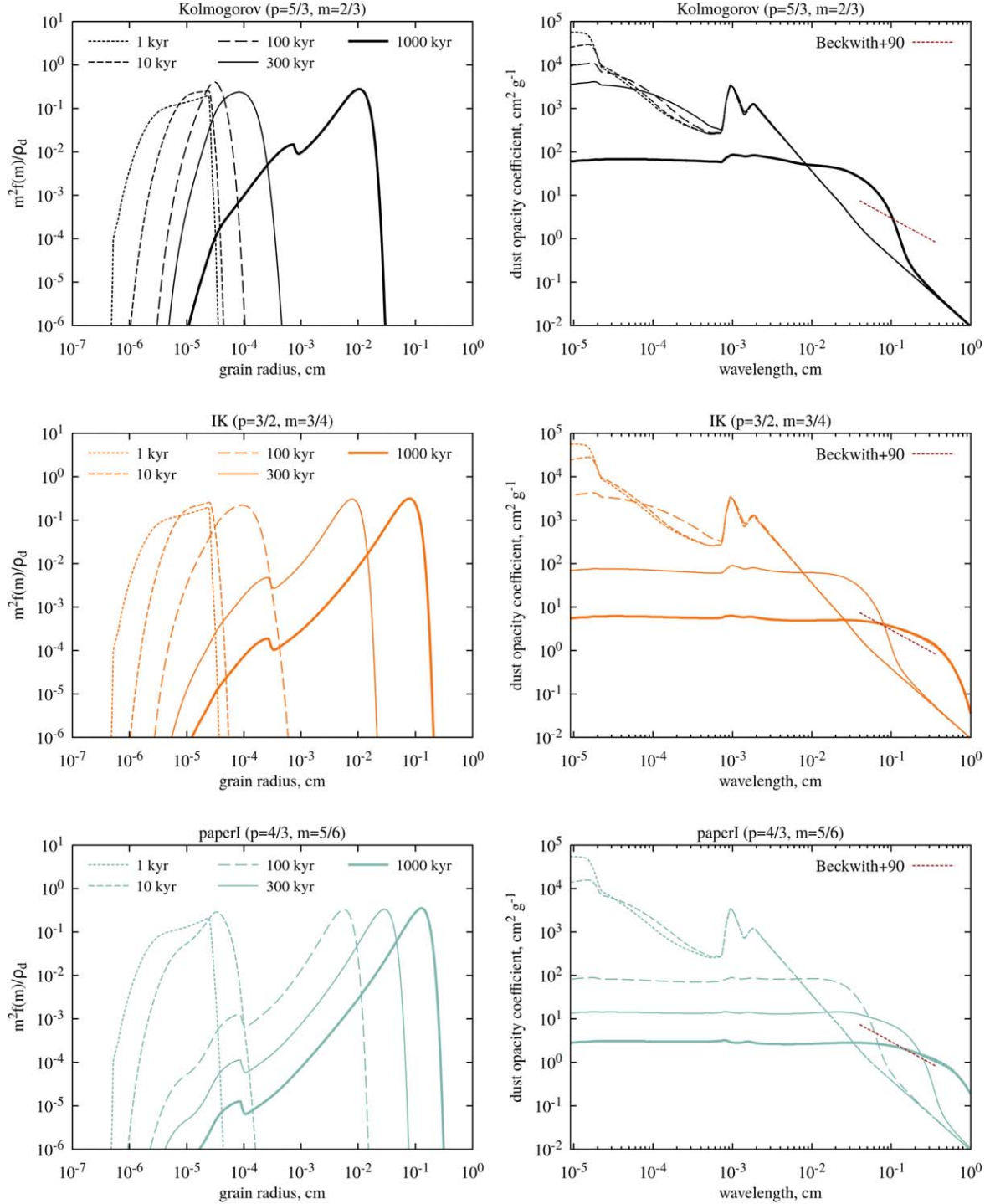






Figure 6. Evolution of the grain size distribution (left) and the corresponding opacity coefficients (right) in the disk midplane at 70 au. The Kolmogorov, IK, and Paper I turbulence cases are shown in the top, middle, and bottom panels, respectively. The red dashed lines in the right panels indicate the opacity coefficients in the millimeter wavelength range by Beckwith et al. (1990).

ORCID iDs

Munan Gong  <https://orcid.org/0000-0003-1613-6263>
 Alexei V. Ivlev  <https://orcid.org/0000-0002-1590-1018>
 Vitaly Akimkin  <https://orcid.org/0000-0002-4324-3809>
 Paola Caselli  <https://orcid.org/0000-0003-1481-7911>

References

- Akimkin, V., Vorobyov, E., Pavlyuchenkov, Y., & Stoyanovskaya, O. 2020a, *MNRAS*, **499**, 5578
- Akimkin, V. V., Ivlev, A. V., & Caselli, P. 2020b, *ApJ*, **889**, 64
- Andrews, S. M. 2020, *ARA&A*, **58**, 483
- Beckwith, S. V. W., Sargent, A. I., Chini, R. S., & Guesten, R. 1990, *AJ*, **99**, 924
- Birnstiel, T., Fang, M., & Johansen, A. 2016, *SSRv*, **205**, 41
- Birnstiel, T., Klahr, H., & Ercolano, B. 2012, *A&A*, **539**, A148
- Birnstiel, T., Ormel, C. W., & Dullemond, C. P. 2011, *A&A*, **525**, A11
- Blum, J., & Wurm, G. 2008, *ARA&A*, **46**, 21
- Brauer, F., Dullemond, C. P., & Henning, T. 2008, *A&A*, **480**, 859
- Draine, B. T., & Lee, H. M. 1984, *ApJ*, **285**, 89
- Epstein, P. S. 1924, *PhRv*, **23**, 710
- Flaherty, K. M., Hughes, A. M., Teague, R., et al. 2018, *ApJ*, **856**, 117
- Goldreich, P., & Sridhar, S. 1995, *ApJ*, **438**, 763
- Gong, M., Ivlev, A. V., Zhao, B., & Caselli, P. 2020, *ApJ*, **891**, 172
- Grete, P., O'Shea, B. W., & Beckwith, K. 2021, *ApJ*, **909**, 148
- Gundlach, B., & Blum, J. 2015, *ApJ*, **798**, 34
- Hayashi, C. 1981, *PTthPS*, **70**, 35
- Iroshnikov, P. S. 1964, *SvA*, **7**, 566
- Ishihara, T., Kobayashi, N., Enohata, K., Umemura, M., & Shiraishi, K. 2018, *ApJ*, **854**, 81
- Ishihara, T., Morishita, K., Yokokawa, M., Uno, A., & Kaneda, Y. 2016, *PhRvF*, **1**, 082403
- Klahr, H. 2004, *ApJ*, **606**, 1070
- Klahr, H. H., & Bodenheimer, P. 2003, *ApJ*, **582**, 869
- Kraichnan, R. H. 1965, *PhFl*, **8**, 1385
- Lesur, G., & Papaloizou, J. C. B. 2010, *A&A*, **513**, A60
- Manger, N., Klahr, H., Kley, W., & Flock, M. 2020, *MNRAS*, **499**, 1841
- Markiewicz, W. J., Mizuno, H., & Voelk, H. J. 1991, *A&A*, **242**, 286
- Mathis, J. S., Rumpl, W., & Nordsieck, K. H. 1977, *ApJ*, **217**, 425
- Nelson, R. P., Gressel, O., & Umurhan, O. M. 2013, *MNRAS*, **435**, 2610
- Okuzumi, S. 2009, *ApJ*, **698**, 1122
- Okuzumi, S., Tanaka, H., Kobayashi, H., & Wada, K. 2012, *ApJ*, **752**, 106
- Ormel, C. W., & Cuzzi, J. N. 2007, *A&A*, **466**, 413
- Pan, L., & Padoan, P. 2015, *ApJ*, **812**, 10
- Petersen, M. R., Julien, K., & Stewart, G. R. 2007, *ApJ*, **658**, 1236
- Pinte, C., Dent, W. R. F., Ménard, F., et al. 2016, *ApJ*, **816**, 25
- Rosotti, G. P., Tazzari, M., Booth, R. A., et al. 2019, *MNRAS*, **486**, 4829
- Sakurai, Y., Ishihara, T., Furuya, H., Umemura, M., & Shiraishi, K. 2021, *ApJ*, **911**, 140
- Segura-Cox, D. M., Harris, R. J., Tobin, J. J., et al. 2016, *ApJL*, **817**, L14
- Segura-Cox, D. M., Looney, L. W., Tobin, J. J., et al. 2018, *ApJ*, **866**, 161
- Segura-Cox, D. M., Schmiedeke, A., Pineda, J. E., et al. 2020, *Natur*, **586**, 228
- Simon, J. B., Bai, X.-N., Flaherty, K. M., & Hughes, A. M. 2018, *ApJ*, **865**, 10
- Stoll, M. H. R., & Kley, W. 2016, *A&A*, **594**, A57
- Testi, L., Birnstiel, T., Ricci, L., et al. 2014, in *Protostars and Planets VI*, ed. H. Beuther et al., 339 (Tucson, AZ: Univ. Arizona Press)
- Völk, H. J., Jones, F. C., Morfill, G. E., & Roeser, S. 1980, *A&A*, **85**, 316
- Youdin, A. N. 2010, in *Physics and Astrophysics of Planetary Systems*, EAS Publications Series, ed. T. Montmerle, D. Ehrenreich, & A. M. Lagrange, 41 (Les Ulis: EDP Sciences), 187
- Youdin, A. N., & Lithwick, Y. 2007, *Icar*, **192**, 588